

# Pore-Engineered Ultrahigh Surface Area Okra-Derived Activated Carbon for Concurrently High-Power-Density and High-Energy-Density Supercapacitor

Ekta Majhi and Atul Suresh Deshpande\*

Simultaneously, high energy and power density are extremely desirable attributes in supercapacitors. Carbon-based supercapacitors deliver high power but cannot retain significant energy density at high charging rates. Herein, it is demonstrated that the prudent selection of okra as a carbon precursor, diligent processing, and use of water-in-salt electrolyte (WiSE) to expand the voltage window ensures both high energy and high-power density. Okra is an ideal carbon precursor as it contains a significant amount of water and minerals. Their methodical removal during processing yields okra-derived activated carbon (OAC), having an ultrahigh surface area of  $2109 \text{ m}^2 \text{ g}^{-1}$  with an effective

combination of micro/meso/macropores. The electrochemical studies of OAC in a three-electrode system using 6 M KOH as an electrolyte display an outstanding capacitance of  $318 \text{ F g}^{-1}$  at  $1 \text{ A g}^{-1}$ . Furthermore, the potential window is extended to 1.6 V using a WiSE (27 molal  $\text{CH}_3\text{COOK}$ ). This leads to a remarkable increase in energy density to  $44.44 \text{ Wh kg}^{-1}$  with an extraordinary power density of  $80,000 \text{ W kg}^{-1}$  at  $50 \text{ A g}^{-1}$  in two-electrode system. 100% capacitance retention is observed after 10,000 cycles at  $10 \text{ A g}^{-1}$ . This study highlights the importance of pore engineering for superior electrochemical performance.

## 1. Introduction

Supercapacitors are of significant interest for energy storage applications for their potential application in electric vehicles and digital devices, owing to their ability to deliver high power, long device lifespans, and capacity to handle high peak currents.<sup>[1]</sup> However, a key challenge hindering their widespread adoption is their relatively low energy density.<sup>[2,3]</sup> Both energy and power characteristics are influenced by material properties such as surface area, pore size distribution, electrical conductivity, and operating voltage range.<sup>[4,5]</sup> Carbon-based materials have been extensively investigated for electric double-layer capacitors (EDLCs) due to their easily tuneable properties, including phase evolution, nature of bonding, heteroatom doping,<sup>[6]</sup> surface area, and pore geometry, which can be optimized through precise precursor selection and processing methods. Various parameters influence the energy density of carbon-based materials. For example, the higher the surface area, the greater the number of active sites for ion adsorption-desorption. Doping with heteroatoms such as N, B, O, and so on can also increase the number of active sites by introducing defects in carbon structure.<sup>[7,8]</sup> Thus, energy density can be improved by the increase in surface area and doping.<sup>[9,10]</sup> However, simply achieving a high surface area is not sufficient to achieve high energy density. The right combination of micro-,

meso-, and macropores enables efficient ion flow, which is needed for capacity retention at high current densities.<sup>[11]</sup> Furthermore, good electrical conductivity of materials is also important for capacity retention. Typically,  $sp^2$  hybridized carbons, such as graphite, graphene, carbon nanotubes,<sup>[12]</sup> and so on, are known to possess good electrical conductivity.<sup>[13]</sup> The nature bonding of these carbon materials is, in turn, dictated by the chemical and morphological properties of carbon precursor and their thermal decomposition behavior. Thus, the choice of carbon precursor and processing parameters are crucial for achieving high energy density. Various reports have shown the influence of processing parameters on electrochemical performance, such as type of activating agent,<sup>[14]</sup> concentration of activating agent,<sup>[15]</sup> precarbonization, and activation temperature.<sup>[16]</sup> Apart from tuning material properties, enhancement in energy density has been achieved by increasing the potential window using various electrolyte systems such as nonaqueous organic electrolytes,<sup>[17]</sup> ionic liquids,<sup>[18]</sup> water-in-salt electrolyte (WiSE).<sup>[19,20]</sup>

Since the electrochemical performance mainly hinges on the material properties, the choice of precursor is of utmost importance. Among carbon precursors, a wide range of plant-based biomass materials have been explored to derive activated carbon, such as watermelon,<sup>[21]</sup> pokeweed leaves,<sup>[22]</sup> agriculture crop waste,<sup>[23]</sup> wood,<sup>[24]</sup> plant tissue,<sup>[25]</sup> coffee,<sup>[26]</sup> sugarcane bagasse,<sup>[27]</sup> orange peel,<sup>[28]</sup> soybean pod,<sup>[29]</sup> bamboo byproducts,<sup>[30]</sup> Hemp stem,<sup>[31]</sup> mushroom,<sup>[32]</sup> tea leaves,<sup>[33]</sup> microalgae,<sup>[34]</sup> and so on. The popularity of biomass precursors lies mainly in their hierarchical structure.<sup>[35]</sup> In addition, biomass-based precursors may contain biomolecules such as protein, lipids, and pigments which can introduce heteroatoms such as N, S, O, P, and so on as dopants in resultant carbon materials. Several biomass materials also contain

E. Majhi, A. S. Deshpande

Department of Materials Science and Metallurgical Engineering  
Indian Institute of Technology Hyderabad  
Sangareddy, Telangana 502284, India  
E-mail: atuldeshpande@msme.iith.ac.in

 Supporting information for this article is available on the WWW under <https://doi.org/10.1002/batt.202500160>

significant amounts of minerals such as  $\text{Na}_2\text{O}$ ,  $\text{Fe}_2\text{O}_3$ ,  $\text{MgO}$ ,  $\text{Al}_2\text{O}_3$ ,  $\text{K}_2\text{O}$ ,  $\text{CaO}$ ,  $\text{SiO}_2$ , and so on<sup>[36]</sup> which turn into ash upon carbonization.<sup>[37]</sup> Removal of ash from carbonized samples can result in enhanced porosity. While all these minerals predominantly act as porogens, some of them may also behave as activating agents or graphitizing agents.<sup>[17,38]</sup>

Activated carbon properties, such as surface area, pore size distribution, voltage range, and electrical conductivity, are highly interdependent, where improving one parameter can compromise others. To achieve both high energy and power density simultaneously in supercapacitors, a strategic combination of precursor selection, electrolyte choice, and processing conditions is necessary. In this study, okra was selected as a precursor for activated carbon due to its hierarchical structure, high water content ( $\approx 90\%$ ) in form of mucilage,<sup>[37,39]</sup> and rich in proteins and mineral,<sup>[40]</sup> which facilitated unique pore engineering during processing. This carefully designed hierarchical porous structure significantly enhances ion transport and charge storage capabilities. The processing steps were designed to optimize porosity and maximize surface area by careful removal of water via freeze-drying and removal minerals (ash) from precarbonized okra sample by acid treatment. To achieve enhanced and uniform activation, precarbonized okra samples were impregnated with KOH solution rather than mixing with solid KOH. The resulting activated carbon exhibited ultrahigh surface area with a balanced distribution of micro-, meso-, and macropores as shown in Figure 1. Electrochemical testing in 6 M KOH demonstrated excellent performance in both three-electrode and two-electrode configurations, achieving high energy and power density. Further performance enhancement was observed using 27 M potassium acetate ( $\text{CH}_3\text{COOK}$ ), which expanded the voltage window to 1.6 V in aqueous system. This strategic choice enhances the energy density but also maintains excellent cycling stability and power performance. This integrated approach offers a scalable route for the design of advanced, biomass-derived supercapacitor materials with enhanced electrochemical properties.

## 2. Results and Discussion

### 2.1. Morphological and Structural Characterization

The choice of Okra as a biomass precursor for activated carbon was made based on its inherent microstructural and compositional properties, which allows pore engineering at various stages. For example, okra possesses a hierarchical porous structure like any other biomass, but in addition it also contains about 11.44 wt% mucilage<sup>[41]</sup> in the form of a hydrogel. It is a mixture of polysaccharides of varied composition with random chain structure and high-water retention capacity ( $\approx 90$  wt%).<sup>[39]</sup> Consequently, drying can result in the collapse of the mucilage network and loss of inherent morphology due to capillary forces exerted by the evaporation of water. Therefore, we employed freeze-drying as it avoids capillary pressure and retains the inherent morphology.<sup>[11]</sup> Figure S1, Supporting Information shows the comparison of morphology of diced pieces oven-dried okra and freeze-dried okra (FDO) at different length scales. It is evident from Figure S1a–c, Supporting Information that oven drying results in significant shrinkage of sample and also collapse of microstructure. In contrast, the freeze-drying process retains the morphology of fresh okra (Figure S1d–f, Supporting Information). Proximate analysis reveals that, through freeze-drying, sliced okra underwent a water reduction of 86.8%, as determined by measuring the weight difference before and after the drying process.

Figure 2 shows the morphology of FDO. The cross-sectional view at low magnification (Figure 2a) reveals large voids (150–200 nm) resulting from the removal of the seeds. A part of the surface of the sample is covered with crumpled sheet like material, which most probably originates due to oozing out of mucilage during sample cutting. Upon closer inspection (Figure 2b), the morphology of this film resembles the morphology of freeze-dried hydrogels with ultrafine pores due to the removal of water.<sup>[42]</sup> The underlying honeycomb structure in

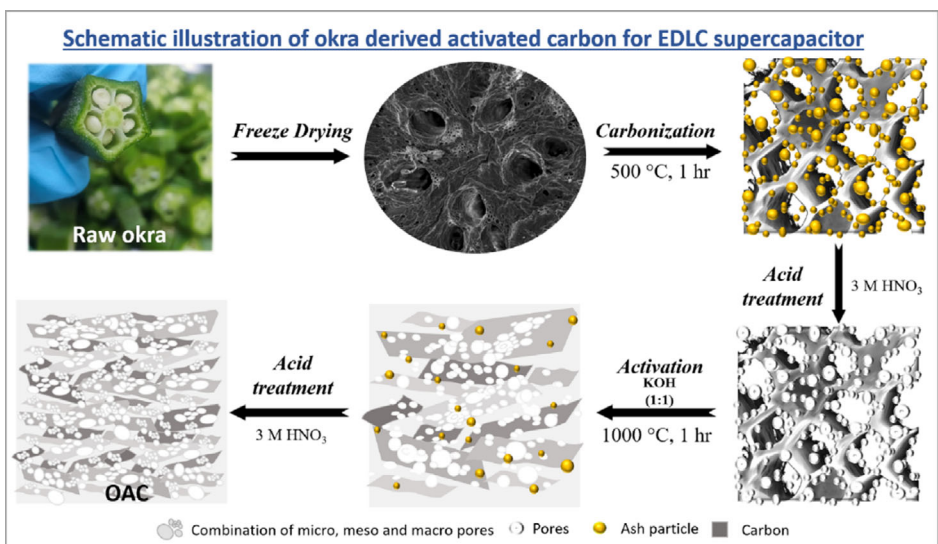


Figure 1. Schematic representation of the synthesis scheme for OAC for electrode fabrication intended for supercapacitor application.

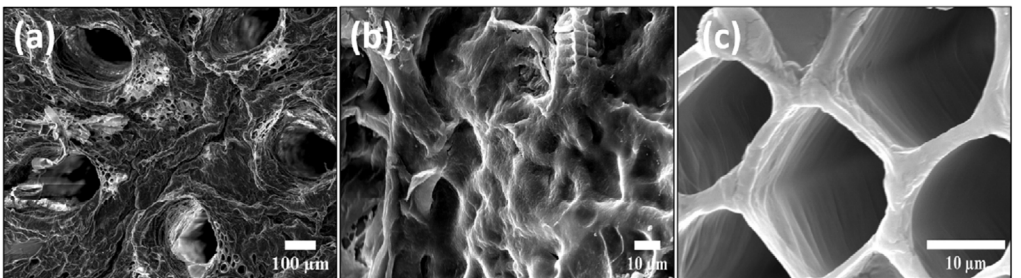


Figure 2. FE-SEM images of FDO at a) low, b) intermediate, and c) high magnification.

FDO is evident in Figure 2c. This honeycomb structure comprises individual cells with cross section of 15–20 nm and thin walls measuring thickness of 2–4 nm. Even after carbonization of FDO at 500 °C, the morphology and microstructure of okra are well retained, as shown in Figure S1g–i, Supporting Information.

After carbonization of samples at 500 °C, the samples were ground to obtain a fine powder. The gross morphology of okra was retained in the powdered form. However, the grinding of samples resulted in the destruction of the honeycomb structure, as seen in the low-magnification scanning electron microscopy (SEM) image of the precarbonized and ground okra sample (OC) depicted in Figure 3a. Nonetheless, large flakes consisting of broken cell walls were evident. During carbonization, reactions like dehydration, decarboxylation, and decarbonization occur.

These reactions also include the conversion of minerals present in okra to ash. Since okra is known to contain a significant amount of minerals (5–11%),<sup>[37]</sup> one can expect the presence of a fair amount of ash in precarbonized samples. To quantify the ash content in our sample, we carried out a thermogravimetric analysis (TGA) of FDO and OC samples which revealed 4.8 wt% and 16 wt% ash content, respectively (Figure S2, Supporting Information). The presence of such a significant amount of ash was evident from a higher magnification image of the OC sample (Figure 3b). The SEM shows that ash is present in the form of a large number of particles dispersed over the sample surface. These particles have a wide particle size distribution ranging from 500 nm to 10 nm range. To verify that these particles are ash particles, we carried out an energy-dispersive X-ray spectroscopy (EDS) analysis.

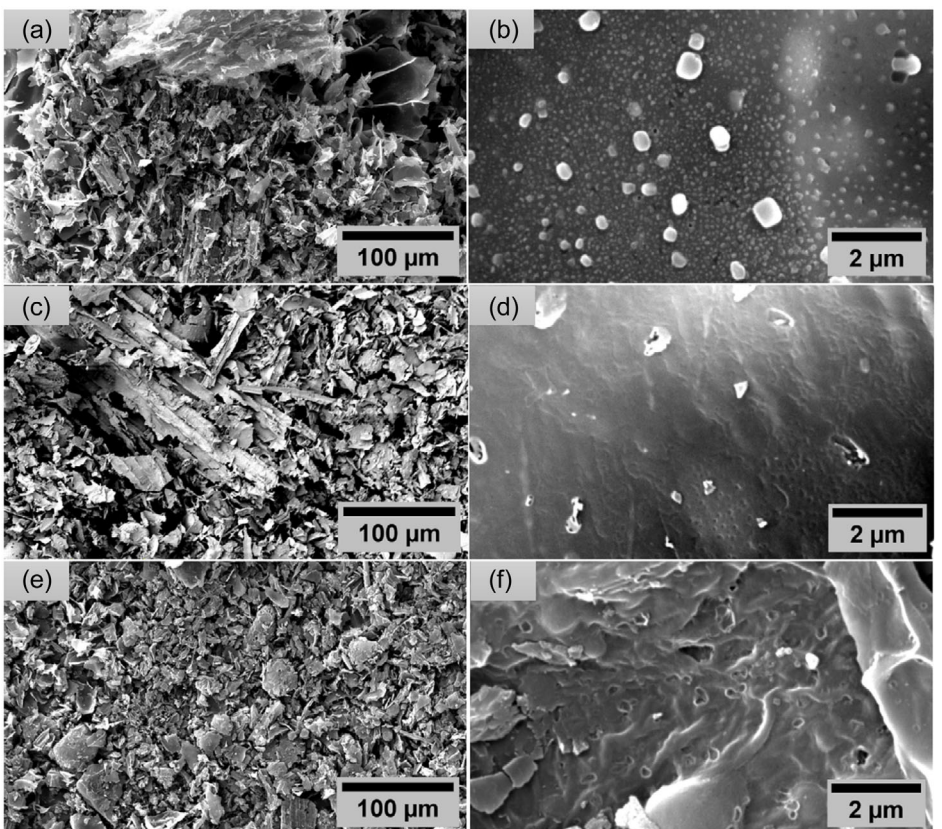


Figure 3. Low- and high-magnification FE-SEM images of a,b) OC, c,d) OAT, and e,f) OAC carbon samples.

In Figure S3, Supporting Information, SEM image of OC sample and its corresponding elemental mapping obtained from EDS analysis clearly show the presence of carbon in atomic percentage (72%), potassium (9%), chlorine (5%), calcium (1.4%), phosphorus (1.5%), and oxygen at (7%). There are localized regions with greater density of elements such as K, Cl, Ca, and O. These regions can be correlated to high contrast particles in SEM images. It proves that these particle are that of mineral ash.

To improve the porosity, these ash particles were leached out by treating the precarbonized samples with 3M HNO<sub>3</sub>. Figure 3c indicates that the sample after acid treatment (OAT) retains the gross morphology of OC. However, the removal of ash particles leads to the generation of a large number of pores (Figure 3d). This improved porosity is important as these pores allow better penetration of the activating agent (KOH) through the carbon matrix. To enhance the effect of the activating agent, we also modified the activation process by aging the OAT samples in concentrated KOH solution rather than the conventional approach of

simple mixing of solid KOH and precarbonized powder before activation. Aging of OAT sample in KOH solution followed by drying in the oven was done to ensure even and more effective impregnation of the precarbonized sample with KOH. This can not only enhance activation but also regulate pore sizes in activated carbon. The SEM images of activated carbon samples obtained by heat treatment at 100 °C (okra-derived activated carbon [OAC]) show that after activation (Figure 3e), the particle size and thickness of carbon flakes reduced to some extent. At higher magnification (Figure 3f), we can clearly observe enhancement in porosity after activation.

Transmission electron microscopy (TEM) analysis of OC, OAT, and OAC samples was carried out to gain deeper insight into the effect of freeze drying, acid leaching, and modified activation process. TEM images reveal the glassy nature of carbon for all samples. **Figure 4a** illustrates the morphology of the OC sample which is similar to carbon derived from various biomass precursors.<sup>[17,28,43]</sup> Figure 4b also confirms the existence of ash particles

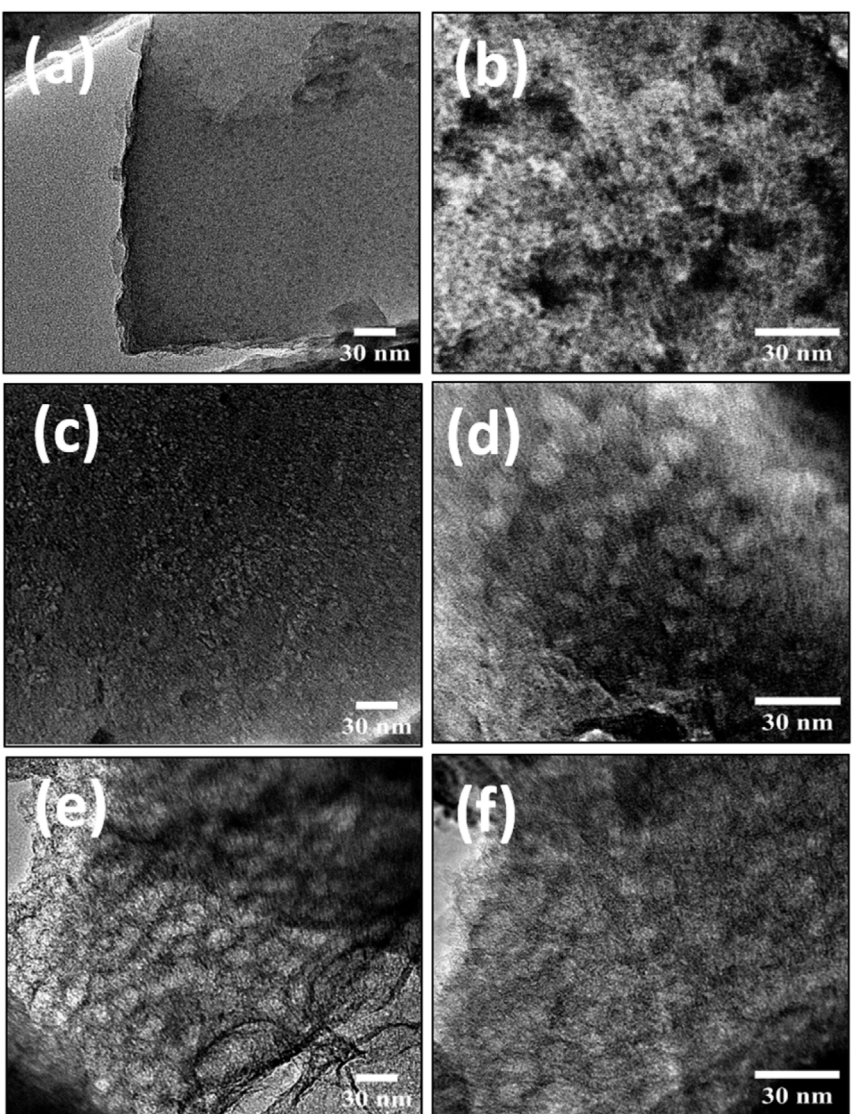


**Figure 4.** Low- and high-magnification TEM images of a,b) OC, c,d) OAT, and e,f) OAC samples.

embedded within the carbon matrix, which appear darker due to their greater electron density. The TEM images of the OAT sample (Figure 4c,d) clearly show the large number of mesopores and micropores that resulted from the leaching of ash particles by acid treatment.

Finally, after KOH activation (OAC), a definite increase in the number of mesopores and micropores is visible in Figure 4e,f. Here, KOH as an activating agent generates the hierarchical porous network by etching amorphous carbon region and facilitates exfoliation forming layered structure. Based on SEM and TEM results we conclude that the removal of minerals by acid treatment and modifying the activation process leads to high porosity with the combination of macro-, meso-, and micropores.

Surface area and pore structure analysis were conducted using  $N_2$  adsorption–desorption isotherm at 77 K, as illustrated in Figure S4a, Supporting Information. All samples exhibit a combination of Type 1 and Type 4, indicating a combination of micro- and mesopores.<sup>[44]</sup> From Table 1 we can see that for the OC sample, the surface area and pore volume are comparatively less. However, the removal of ash by acid treatment leads to a more than 20-fold increase in surface area and a tenfold increase in pore volume. The increase in surface area and pore volume was anticipated since the OC sample contained a significant amount of ash (16 wt%), as discussed previously (Figure S2, Supporting Information). The pore size distribution for OAT (Figure S4b, Supporting Information), Table 1 shows that ash removal results in the generation of mesopores. Since the Brunauer–Emmett–Teller (BET) method is not sensitive to quantitative assessment of macropores, the actual porosity may be larger. After activation, we see an astounding increase in surface area of OAC sample from  $41\text{ m}^2\text{ g}^{-1}$  to  $2109\text{ m}^2\text{ g}^{-1}$ . We attribute this dramatic increase in surface area to two processing conditions we adopted: first, the removal of ash by acid treatment generated numerous interconnected meso- and macropores; second, the impregnation of the precarbonized sample with KOH solution during the preparation of a sample for activation. Instead of mixing solid KOH with precarbonized samples, sustained aging in KOH allowed uniform and more effective permeation of KOH through the carbon matrix. This resulted in better activation of carbon samples. Furthermore, for the OAC sample, we see that the processing approaches not only enhanced the surface area but also allowed the generation of a significant fraction of mesopores ( $\approx 40\%$ ) along with micropores ( $\approx 60\%$ ).

Generally, biomass-derived activated carbons predominantly possess micropores which provide more active sites for ion adsorption. Thus, the specific capacitance of microporous

samples is usually high at low charging rates. However, when the charging rate is increased, capacitance decreases because of slower kinetic of electrolyte diffusion through microporous material. It is known that the presence of mesopores can reduce the diffusion distance and improve the kinetic, whereas macropores act as reservoirs for electrolytes. Hence, a proper proportion of micro-, meso-, and macropores is needed to enhance the electrochemical performance by enabling rapid electrolyte transport through the carbon matrix.<sup>[11]</sup> The results so far show that the methodology devised by us was successful in achieving the optimal hierarchical porosity and high surface area.

Apart from porosity, good electrical conductivity is an important attribute of electrode material. The electrical conductivity depends to a large degree on crystallinity and the nature of bonding. To gain insight in this aspect, we carried out X-ray diffraction (XRD) and Raman studies of all the samples. In Figure 5a, all XRD patterns exhibit two broad peaks at  $2\theta$  values of  $25^\circ$  and  $43^\circ$ , corresponding to the (002) and (100) reflections (ICDD card no. 41-1487). The broadness of these reflections indicates poor crystallinity and lack of long-range order, which is the typical nature of glassy carbon.<sup>[45]</sup> The XRD pattern of the OC sample shows several sharp reflections overlaid with broad reflections of glassy carbon. These sharp reflections match with standard XRD patterns of potassium chloride (KCl; ICDD card no. 01-074-9685) and calcium carbonate ( $\text{CaCO}_3$ ; ICDD card no. 05-005-0586), as shown in Figure S5, Supporting Information. The presence of these minerals substantiates the results from EDS analysis that the minerals present in okra transform into ash upon carbonization. The XRD pattern of the acid-treated sample (OAT) shows a complete absence of these mineral reflections, which confirms the removal of the mineral ash by acid treatment.

To assess the nature of bonding and local structural order, Raman spectroscopy studies were carried out. In Figure 5b, the Raman spectra of carbon samples reveal the presence of a band at  $1581\text{ cm}^{-1}$ , which is known as the characteristic of the G band corresponding to  $E_{2g}$  phonon mode. The G band is indicative of  $sp^2$  hybridization carbon.<sup>[46]</sup> A second prominent band at  $1350\text{ cm}^{-1}$  corresponds to the D band, which signifies the presence of defects in the  $sp^2$  network. The intensity ratio  $I_D/I_G$ , calculated by integrating the area under the curves, serves as a measure of the degree of disorder in the  $sp^2$  network. Interestingly, the Raman spectrum for OC exhibits a low  $I_D/I_G$  ratio (2.02) as compared to the  $I_D/I_G$  ratio of the OAT sample (2.53). This can be explained based on the presence of mineral ash particles within the carbon network in the case of OC samples. We believe that the intensity of the D band is less due to the interaction of carbon atoms with the mineral particles which restrict the phonon vibrations giving rise to the D band. Upon acid treatment, the mineral particles are leached out leaving behind pores or defects. These defects enhance the D band intensity considerably. Additionally, the presence of dopants such as nitrogen can also introduce defects within the carbon framework and contribute to D band intensity.<sup>[47]</sup> Subsequent activation of OAC results in a reduction of the  $I_D/I_G$  ratio to 2.36, indicating an etching of disordered carbon by KOH during activation.<sup>[38]</sup> Nevertheless, the high value  $I_D/I_G$  ratio suggests the presence of numerous defects and a significant number of micropores,<sup>[48]</sup> which aligns with the

**Table 1.** Specific surface area, pore volume, micropore, and mesopore volume of OC, OAT, and OAC samples.

Sample name	Specific surface area [ $\text{m}^2\text{ g}^{-1}$ ]	Pore volume [ $\text{cc g}^{-1}$ ]	Micropore volume [ $\text{cc g}^{-1}$ ]	Mesopore volume [ $\text{cc g}^{-1}$ ]
OC	2.3	0.003	0.00012	0.0029
OAT	41.5	0.039	0.009	0.029
OAC	2109	1.091	0.663	0.428

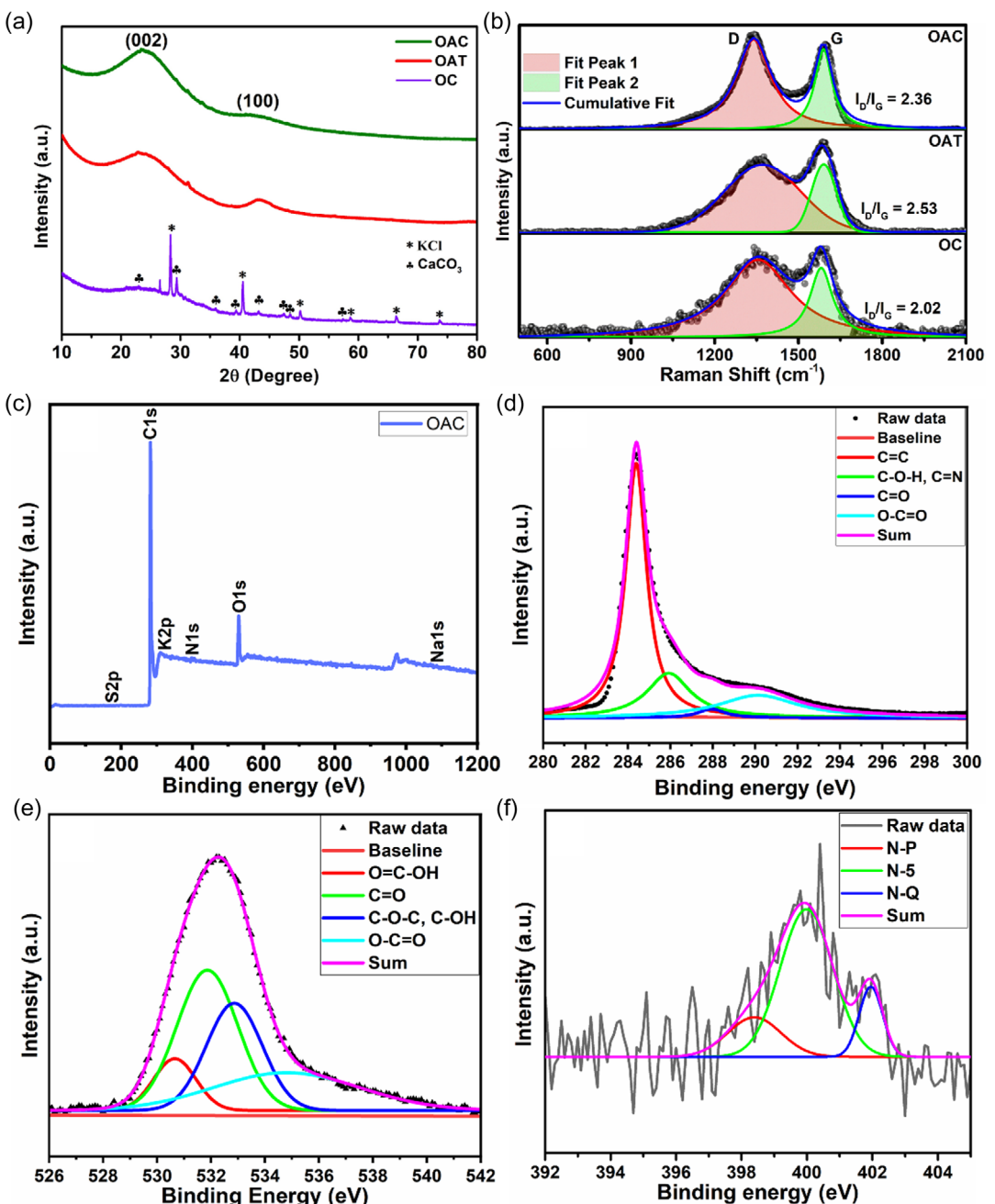


**Figure 5.** a) XRD patterns, b) Raman spectra of OC, OAT, and OAC samples, and c) wide scan XPS spectrum and fine scan spectra d) C1s, e) O1s, and f) N1s of OAC sample.

observation of a substantial amount of micropores in OAC via BET analysis. Such increment in carbon structural defects is likely to enhance active sites or active surface area, thereby potentially boosting the capacitance.<sup>[49]</sup>

Assessment of chemical composition, codoped element concentration, nature of bonding, and structural evolution of activated carbon has been done by X-ray photoelectron spectroscopy (XPS). Figure 5c shows the wide scan XPS spectrum of the OAC sample. The corresponding quantitative elemental assessment is given in Table S1, Supporting Information. The spectrum indicates the presence of carbon as a major component (90%), along with the small atomic percentage of oxygen and

nitrogen. The presence of nitrogen can be attributed to proteins present in okra. In addition, trace amounts of sulfur and potassium were also observed, which could be attributed to remnants of mineral ash after acid treatment. The C1s carbon spectrum shown in Figure 5d can be deconvoluted into 284.3, 285.8, 287.9, and 290.2 eV that are assigned to the C=C, C—O—H, C=N, C—O, and O—C=O, respectively. It is evident from the C1s spectrum that the majority of carbon exists in C=C and C=N bonding, indicating that carbon predominantly exists in  $sp^2$  form with extended  $\pi$  network.<sup>[50]</sup> The O1s spectrum in Figure 5e shows peaks at 530.6, 531.8, 532.2, 532.8, and 534.9 eV are assigned to O=C—OH, C=O, C—O—C, C—OH, and O—C=O,

respectively. All these peaks indicate that oxygen is not part of the carbon framework but exists in the form of functional groups on the surface of the activated carbon.<sup>[51,52]</sup> Further, Figure 5f shows the presence of  $sp^2$  nitrogen containing functional groups such as pyridinic-N (N-P) ( $\approx 398.39$  eV), pyrrolic-N (N-5) ( $\approx 399.98$  eV), and quaternary-N (N-Q) ( $\approx 401.95$  eV). Nitrogen in these groups exists as 5 or 6 membered rings, where a nitrogen atom is in the graphitic carbon network. Nitrogen present in N-5 and N-X forms is known to create pores in hexagonal carbon networks. Therefore, these configurations lead to structural defects, which provide additional sites for ion adsorption while charging and discharging of active material.<sup>[51]</sup> Due to extremely low concentrations of S (0.1 atomic%), K (0 atomic%) and Na (0.1 atomic%), the XPS spectra of these elements exhibit significant noise and lack proper resolution, as illustrated in Figure S6a, b,c, Supporting Information). Given the minimal presence of Na, S, and K in our sample, they do not substantially influence the electrochemical behavior of the OAC sample.

XPS analysis confirmed the presence of pyrrolic and pyridinic type of nitrogen, which are well known for contribution of pseudocapacitance behavior through reversible redox activity. A significant presence of oxygen functional groups, specifically hydroxyl and carbonyl species, was also identified, which improves accessibility of ions, surface polarity, and redox reactions. These surface functionalities play an important role in the overall charge storage mechanism. Among various nitrogen species, pyrrolic-N and quaternary (graphitic-N) groups enhance pseudocapacitive behavior due to their capability to facilitate transfer of electrons and provide chemically active sites. Particularly, the presence of graphitic-N leads to the enhancement of electronic conductivity of the carbon matrix, while pyrrolic-N and pyridinic-N contribute to Faradaic charge storage. Electrochemical measurements further support these observations. The cyclic voltammetry (CV) curves of the oxygen/nitrogen codoped carbon samples reveal broad redox humps and almost rectangular shapes at lower scan rates, indicating electrical double layer (EDL) capacitance and pseudocapacitance simultaneously. At low current densities, the galvanostatic charge-discharge (GCD) profiles are almost isosceles triangles with slight distortions, further validating the efficient ion accumulation and reversible nature of the redox processes. The resulting

pseudocapacitance is primarily attributed to nitrogen (pyridinic and pyrrolic) functional groups and redox-active oxygen (hydroxyl and quinone). Moreover, electrochemical impedance spectroscopy (EIS) depicts low charge transfer resistance, suggesting improved ion transport and enhanced electronic conductivity, due to the synergistic effect of N and O doping in carbon matrix. The excellent cycling stability also reflects the chemical stability and robust structural imparted by these heteroatoms.<sup>[53]</sup> From both Raman and XPS data, we expect good electrical conductivity due to the  $sp^2$  nature of carbon. In addition, the presence of nitrogen in the  $sp^2$  framework can provide additional active sites that can enhance EDLC behavior. The presence of oxygen containing surface functional groups can contribute to a pseudocapacitive nature. However, compared to carbon, the fraction of oxygen is significantly less; therefore, we expect the OAC sample to show predominantly EDLC behavior.

## 2.2. Electrochemical Performance

Electrochemical performance of OAC samples was evaluated by CV, GCD, EIS, and cyclic stability in a three-electrode and two-electrode system using a 6 M KOH electrolyte and further to enhance energy density, operation voltage window widened by using WiSE electrolyte, 27 molal  $\text{CH}_3\text{COOK}$ .<sup>[54]</sup>

CV provides valuable information on the electrochemical behavior of the samples, such as the operating potential window and kinetics of the electrochemical reaction. The results shown in Figure 6a depict a comparison of CV of the OAC sample in 6 M KOH electrolyte at low ( $2\text{--}25\text{ mV s}^{-1}$ ). A potential window of 1 V between  $-0.9\text{ V}$  and  $0.1\text{ V}$  was found to be a suitable range. Beyond  $-0.9\text{ V}$ , we observed a noticeable polarized peak indicating electrolyte decomposition. However, within the potential window, OAC electrodes exhibited high symmetry and reversibility across different scan rates. At low scan rates of  $2\text{--}25\text{ mV s}^{-1}$ , the CV curves are quasirectangular in shape, with broad peaks due to redox reactions possibly involving surface functional groups of the OAC sample, as seen from XPS analysis. Typically, two distinct types of electrochemical reactions can be deduced based on CV analysis. The capacitance is due to the formation of an EDL which is regulated by surface kinetic control. The other type is redox or faradaic reactions, which

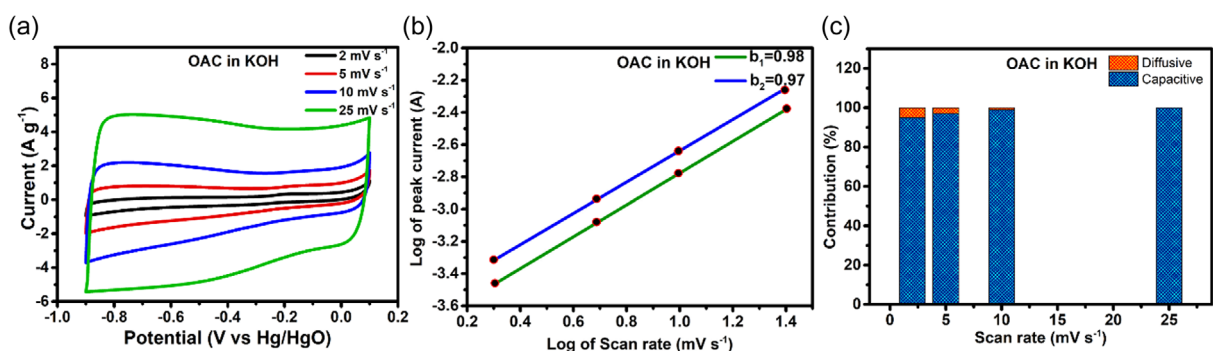


**Figure 6.** Electrochemical characterization of OAC electrode performed in 6 M KOH aqueous electrolyte: a) CV curves at low scan rates from  $2\text{ mV s}^{-1}$  to  $25\text{ mV s}^{-1}$ , b) determination of  $b$  values by CV curves at low scan rates, and c) contribution of surface- and diffusion-controlled capacitance with increasing scan rate in three-electrode setup.

contribute to pseudocapacitance, which is regulated by diffusion- and surface-controlled kinetics. Typically, diffusion-controlled reactions occur at a slower rate, and their dominance can result in poor rate capability. We conducted an electrochemical kinetic analysis to gain insight into the charge storage mechanism of the OAC electrode. As stated in Equation (1), the response current  $i$  is the sum of surface-controlled current  $i_{\text{surface}}$  and diffusion-controlled current  $i_{\text{diffusion}}$ . The response current can also be presented in the form of power law Equation (2), and it is depicted in linear form by Equation (3), taking log on both sides. The scan rate is denoted by  $v$  in  $\text{mV s}^{-1}$ , whereas  $a$  and  $b$  are adjustable parameters.

$$i = i_{\text{surface}} + i_{\text{diffusion}} \quad (1)$$

$$i = av^b \quad (2)$$

$$\log i = \log a + b \log v \quad (3)$$

The values of  $a$  and  $b$  can be deduced from a plot of  $\log i$  versus  $\log v$ . If the value of  $b$  is close to 0.5, it indicates semi-infinite diffusion-controlled kinetics in electrochemical performance, and the current response is proportional to the square root of the scan rate ( $i \propto v^{1/2}$ ). Such a response is typical for battery-like materials. Whereas if the  $b$  value is equal to 1, the current response will be linearly proportional to the scanning rate ( $i \propto v$ ), which is characteristic of surface-controlled behavior. This is the typical behavior of capacitive materials. Thus, the power law allows quick determination of electrode kinetics.  $b$ -values between 0.5 and 1 are transition areas from battery-like (diffusion-controlled process) to capacitive-like responses (surface-controlled process). If the  $b$  value is between 0.85 and 1, surface reactions play a dominant role over diffusion-controlled reactions. Figure 6b depicts the  $\log i$  versus  $\log v$  for cathodic (blue plot) and anodic (green plot) sweeps at slow scan rates. The  $b$  values calculated from the slope of these plots are  $b_1$  (0.98) and  $b_2$  (0.97), cathodic and anodic sweeps, respectively. Since the values of  $b$  in both cathodic and anodic sweeps are close to 1, we conclude that the surface-controlled kinetics dominates during the charge-discharge process.

To quantify the contribution of surface-controlled capacitive (EDLC type) and diffusion-controlled capacitive (pseudotype) mechanisms in overall capacitance, the following equation was used:

$$i(V) = k_1v + k_2v^{1/2} \quad (4)$$

in the form of linear equation can be written as

$$i(V)/v^{1/2} = k_1v^{1/2} + k_2 \quad (5)$$

where  $i(V)$  is the current response value at a fixed voltage  $V$ ,  $k_1v$  corresponds to the surface-controlled process, and  $k_2v^{1/2}$  corresponds to the diffusive process. Using the above equation, adjustable parameters  $k_1$  and  $k_2$  at specific voltage were obtained by plotting  $i(V)/v^{1/2}$  Vs  $v^{1/2}$ .<sup>[5]</sup> Figure 6c shows a representation of the quantitative contributions of both mechanisms observed for the OAC sample using Equation (4) and (5). At a low scan rate ( $2 \text{ mV s}^{-1}$ ), the surface-controlled capacitive contribution (EDLC)

is 95%, which further increases to 99% at a  $10 \text{ mV s}^{-1}$  scan rate. At scan rate  $25 \text{ mV s}^{-1}$  and above, purely EDLC contribution is observed. Such high EDLC contribution can be attributed predominantly to the  $sp^2$  nature of carbon and a minuscule proportion of functional groups, as mentioned previously in the discussion on Raman and XPS data. The functional groups such as carbonyl, carboxyl, and alcohol can undergo redox reactions and contribute to diffusion-controlled (pseudocapacitance) processes.<sup>[55]</sup> Finally, at high scan rates the OAC sample shows 100% EDLC type storage. Compared to the values reported in the literature, OAC gives far better surface charge storage kinetics.<sup>[5,52]</sup> Since the kinetics of surface-controlled EDLC reaction is more rapid than diffusion-controlled pseudocapacitive reaction, we expect that the OAC samples would show better rate capability.

CV was carried out across a range of scan rates from 2 to  $200 \text{ mV s}^{-1}$  as shown in Figure 7a. At low scan rates, the CV curves exhibit slight deviations from the ideal rectangular shape due to faradaic reactions and ion diffusion into deeper pores. Activated carbon typically exhibits a hierarchical porous structure, including micropores that require more time for electrolyte ions to access. The slower scan rates allow sufficient time for ions to penetrate these micropores and interact with surface functional groups, resulting in additional pseudocapacitive contributions, as supported by the XPS analysis discussed earlier. In contrast, at higher scan rates ( $50$ – $200 \text{ mV s}^{-1}$ ), the CV curves maintain a nearly ideal rectangular shape, indicative of dominant EDL capacitive behavior with minimal resistive contribution from the electrode material.<sup>[56]</sup> To study the influence of hierarchical porous structure and activation parameters of OAC on the ion kinetics and charge transfer at the electrode-electrolyte interface, EIS spectroscopic analysis of the OAC sample was carried out. Figure 7b displays the Nyquist plot of OAC. The current response is measured in terms of impedance in the frequency range of  $0.01$ – $10\,000 \text{ Hz}$ . At low frequencies, the reactive component, i.e., the imaginary part of impedance, keeps on increasing. The nearly vertical lines observed at lower frequencies signify a pure capacitive behavior with low diffusion resistance. At a moderate-frequency level, the quasidiagonal line corresponds to the Warburg impedance ( $R_w$ ) associated with the rate of ion diffusion in a porous structure. At moderate frequency, a slope between  $45^\circ$  and  $90^\circ$  can indicate diffusion-related issues, often due to poorly accessible micropores or narrow pore networks. The short length of this region indicates easy ion mobility which is due to hierarchical structure. At the same time, the EIS curve manifests a semicircle at a high frequency, associated with charge transfer resistance ( $R_{ct} = 0.18 \Omega$ ). Generally, a purely EDLC type of supercapacitor should not yield a semicircle in the EIS curve, as there are no charge transfer events. However, the presence of semicircle indicates charge transfer reactions may be due to redox reactions involving surface functional groups and doped nitrogen, as shown previously by XPS and EDS analysis.<sup>[56]</sup> The heteroatoms present in activated carbon improves surface chemistry and wettability as well as also contribute to both EDLC and pseudocapacitance through different mechanisms. Nitrogen doping substitutes carbon atoms with nitrogen, which has five valence electrons compared to four carbon atoms. This incorporates extra electrons in the system, which improves electrical conductivity of

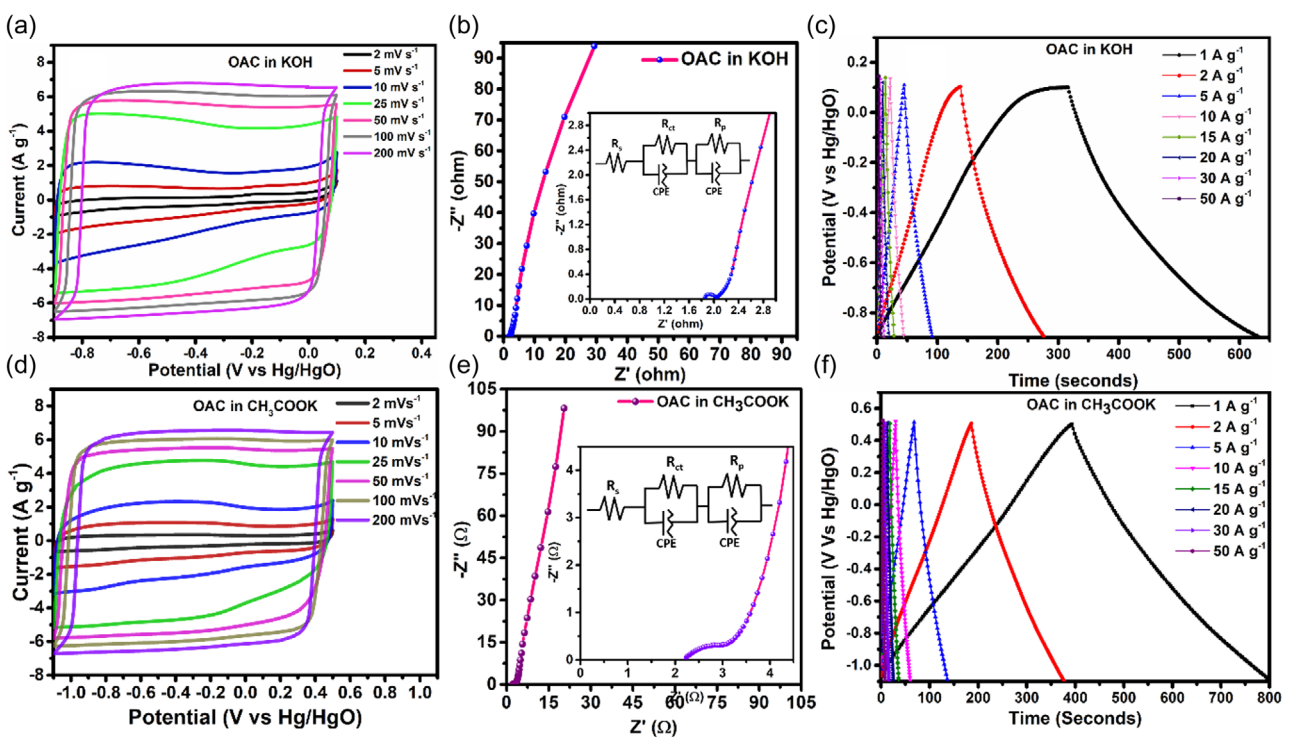


**Figure 7.** Electrochemical characterization of OAC electrode performed in 6 M KOH aqueous electrolyte and 27 M CH<sub>3</sub>COOK aqueous WSe electrolyte: a) CV curves at low scan rates from 2 mV s<sup>-1</sup> to 200 mV s<sup>-1</sup>, b) Nyquist plot and (inset plot highlighting high-frequency region and electrochemical equivalent circuit model for EIS spectra), and c) GCD curves from 1 A g<sup>-1</sup> to 50 A g<sup>-1</sup> current density, for OAC in KOH in three-electrode setup. Comparison with d) CV curves from 2 mV s<sup>-1</sup> to 200 mV s<sup>-1</sup> scan rate, e) Nyquist plot and (inset plot highlighting a high-frequency region and electrochemical equivalent circuit model), and f) GCD curves from 1 A g<sup>-1</sup> to 50 A g<sup>-1</sup> current density tested in CH<sub>3</sub>COOK aqueous WSe electrolyte in three-electrode setup.

the electrode material. Due to its smaller higher electronegativity and atomic radius, nitrogen permits higher dopant concentrations and therefore enhances the surface wettability by promoting stronger interactions with electrolyte ions. Nitrogen can be present in the carbon structure in various forms. Among them, pyridinic and pyrrolic nitrogen, located at the defects or edges of graphene layers, contribute to pseudocapacitance through redox reaction, while quaternary nitrogen integrated into the graphitic lattice improves electrical conductivity and facilitates transfer of electron during electrochemical reactions. Oxygen heteroatom doping into the bulk material introduces polar functional groups that significantly increase the hydrophilicity, thereby improving the electrolyte infiltration and enhancing wettability of the porous carbon. The mass transfer resistance decreases due to the improvement in ion transport which supports efficient EDL formation at the electrode electrolyte interface, hence enhancing the overall electrochemical performance.<sup>[57]</sup> Alternately, the semicircle can also originate from interfacial resistance between current collector and electrode material. Bulk solution resistance ( $R_s = 1.86 \Omega$ ) of electrolyte incorporates between the reference and counter electrode, which is relatively small.<sup>[56,58]</sup> Overall, the impedance behavior can be represented by an equivalent circuit given in the inset of Figure 7b. After the basic electrochemical characterization, such as CV and EIS, the GCD study was carried out to assess the electrochemical performance of the OAC sample. Typically, GCD gives valuable information about specific capacitance and rate

capability. In addition, the shape of GCD curves reveals the mechanism of electrochemical reactions taking place. Figure 7c demonstrates GCD curves obtained for the OAC sample at current densities of 1 A g<sup>-1</sup>–50 A g<sup>-1</sup>. Almost triangular shape of GCD curves indicates that the charge storage happens predominantly via EDL formation. A high capacitance of 318 F g<sup>-1</sup> was obtained at a current density of 1 A g<sup>-1</sup>, calculated using equation (6). Such high values can be attributed to the ultrahigh surface area of OAC samples. Furthermore, defects formed due to nitrogen doping provide additional active sites adsorption of electrolyte ions, as mentioned in the previous section. At high current density, i.e., 50 A g<sup>-1</sup>, the OAC electrode delivers 160 F g<sup>-1</sup>. Table S2, Supporting Information shows values of the specific capacitance of the OAC sample in KOH electrolyte with increasing current densities. The comparison of corresponding energy densities and power densities indicates high rate capability. The high rate capability can be mainly attributed to the purely EDLC charge storage mechanism observed for OAC samples. The hierarchical porous structure of OAC with an optimum combination of micro-, meso-, and macropores also aids in capacity retention by allowing better flow kinetics.<sup>[59]</sup> Excellent coulombic efficiency of 100% was obtained at all current densities. The cyclic stability of OAC samples at a high current density of 10 A g<sup>-1</sup> was assessed for 10,000 cycles. Figure S7, Supporting Information depicts that OAC exhibits excellent cyclic stability with 100% capacity retention at a steady capacitance of 220 F g<sup>-1</sup> with 100% coulombic efficiency. We attribute this

remarkable performance to a culmination of low material impedance, dominant EDLC behavior, and structural and chemical stability of the OAC samples.<sup>[57,58,60]</sup>

The energy density of supercapacitors is directly proportional to square of voltage window used. Thus, in order to improve voltage window, we must increase the stability of the electrolyte. For aqueous electrolytes, one can get a maximum voltage of 0–1.23 V. Beyond this potential window, water undergoes electrolysis. One of the ways to improve the stability of water-based electrolytes is to use WiSEs.<sup>[55]</sup> WiSEs are highly concentrated (typically saturated solutions) aqueous salt solutions. Usually, salts with extremely high solubilities are used for WiSE system. Thus, WiSEs comprise less amount of water than salt. Consequently, nearly all the water molecules in these solutions are tightly bound to electrolyte ions to keep the electrolyte ions in solvated state. Hence, these solutions lack free water molecules. Due to the strong interaction between water molecules and electrolyte ions, the water molecules do not undergo electrolysis within the usual potential window of 1.23 V. This allows the extension of the potential window of such aqueous solutions beyond 1.23 V.<sup>[20,55]</sup> The extent of increase in potential window is dependent on properties of individual electrolytes such as solubility of salts and electrochemical stability of electrolyte ions. We employed 27 molal( $\text{mol kg}^{-1}$ )  $\text{CH}_3\text{COOK}$ , i.e., saturated solution of  $\text{CH}_3\text{COOK}$  as a WiSE for our experiments. Examination of the CV plots of OAC in 27 molal  $\text{CH}_3\text{COOK}$  electrolyte in three-electrode setup, as shown in Figure 7d, reveals that CV curves show a pure EDLC type of charge storage mechanism with increase in scan rate. The use of WiSE electrolyte yielded a wider potential window of 1.6 V (−1.1 V to 0.5 V), as compared to 1 V observed with KOH as an electrolyte. The Nyquist plot depicted in Figure 7e illustrates very low charge transfer resistance ( $R_{ct} = 0.7 \Omega$ ) and slightly elevated solution resistance ( $R_s = 2.2 \Omega$ ). This lowered resistance is attributed to the abundance of ions available within an effective distance. However, the comparatively higher  $R_s$  can be attributed to the large ionic size and high concentration, which results in greater ion–ion interactions. This hinders the movement of ions and increases solution resistance. Notably, the quarter circle observed instead of a semicircle suggests limited ion diffusion. Examination of the EIS plot at low frequencies highlights the significant effect of the EDLC charge storage mechanism.<sup>[61]</sup> In Figure 7f, the triangular GCD plot demonstrates symmetric and highly reversible charge–discharge cycles. A specific capacitance of  $256 \text{ F g}^{-1}$  is achieved at a current density of  $1 \text{ A g}^{-1}$ . The lesser specific capacitance obtained using  $\text{CH}_3\text{COOK}$  as an electrolyte compared to capacitance obtained using KOH may be due to the inability of  $\text{CH}_3\text{COO}^-$  ions to enter ultramicropores due to their larger ionic radius.

To assess the electrochemical behavior of the OAC electrodes sample at device level, a Swagelok cell consisting of symmetric two-electrode setup was assembled. Figure S8a, Supporting Information presents the CV of OAC electrodes in a 6 M KOH electrolyte at scan rates ranging from 5 to 200 mV s<sup>−1</sup> within a potential window of 0–1 V in a two-electrode system. The OAC electrodes maintain high reversibility across all scan rates. The CV curves display a quasirectangular shape that highlights capacitive behavior of OAC symmetric device. Similar behavior is

observed in three-electrode setup at low scan rates. While, here in two-electrode setup along with the low scan rates quasirectangular nature persists even at high scan rates, which suggests that the resistive behavior originates from slow ionic diffusion in the diffused layer. This can be attributed to increase in solution resistance caused by the restricted movement of ions across the separator as evident from EIS spectroscopy. Figure S8b, Supporting Information shows the Nyquist plot of OAC in a two-electrode system over a frequency range of 0.01–10,000 Hz, compared to three-electrode setup EIS spectrum of OAC in two-electrode setup distinct difference arises due to change in setup. For instance, the solution resistance increased to  $3.7 \Omega$  for two-electrode system compared to three-electrode system ( $1.8 \Omega$ ). This may be attributed to the separator as stated above. The literature reports show that separator properties such as porosity, pore size, and wettability can impede ion movement, leading to an increase in solution resistance.<sup>[61]</sup> A semicircle observed at high frequencies corresponds to the charge transfer resistance ( $R_{ct} = 0.51 \Omega$ ). A near-90° slope of EIS curve at lower frequency region represents ideal capacitive behavior, where ions quickly form a double layer without significant resistance. Figure S8c, Supporting Information demonstrates GCD curves obtained for the OAC sample at current densities of  $1\text{--}50 \text{ A g}^{-1}$ . Perfect triangular shape of GCD curves indicates pure EDL formation. A high capacitance of  $216 \text{ F g}^{-1}$  was obtained at a current density of  $1 \text{ A g}^{-1}$  using Equation (7). The energy density and power density calculated using Equation (8) and (9) were found to be  $30 \text{ Wh kg}^{-1}$  and  $1000 \text{ W kg}^{-1}$ , respectively. At a high current density, i.e.,  $50 \text{ A g}^{-1}$ , the OAC electrode delivers a capacitance of  $168 \text{ F g}^{-1}$ , with a corresponding high energy density of  $23.3 \text{ Wh kg}^{-1}$  and an exceptionally high power density of  $50 \text{ kW kg}^{-1}$ . Such high values can be attributed to purely EDLC behavior of OAC. Excellent coulombic efficiency of 100% was observed for all the GCD curves. The cyclic stability of OAC samples at a high current density of  $10 \text{ A g}^{-1}$  was assessed for 10,000 cycles. Figure S8d, Supporting Information depicts that OAC exhibits cyclic stability with 88% capacity retention at a steady capacitance of  $192 \text{ F g}^{-1}$  with 100% coulombic efficiency. In the cyclic stability analysis, the capacitance decreased to  $176 \text{ F g}^{-1}$  at the 1500th cycle and remained relatively stable until the 7600th cycle, after which it dropped further to  $168 \text{ F g}^{-1}$ . This subsequent reduction in capacitance may be attributed to the decomposition of the electrolyte, which can lead to gas evolution at electrode–electrolyte interface. The generated gas disrupts the electrode–electrolyte interface, diminishes effective surface area of electrode, and affects the electrochemical performance with increase in charge–discharge cycles.<sup>[62,63]</sup>

In two-electrode setup, 1.6 V potential stability window is maintained, without any parasitic reaction as shown in Figure 8a. The quasirectangular shape of CV curves indicates prominent surface-controlled charge storage with inconspicuous contribution of diffusion-controlled storage similar to the CV curves obtained using KOH as an electrolyte. As the scan rate increases, CV curves exhibit resistive behavior in EDLC type of charge storage mechanism. Nyquist plot depicted in Figure 8b illustrates slightly elevated solution resistance ( $R_s = 5.8 \Omega$ ). However, the comparatively higher  $R_s$  can be attributed to the

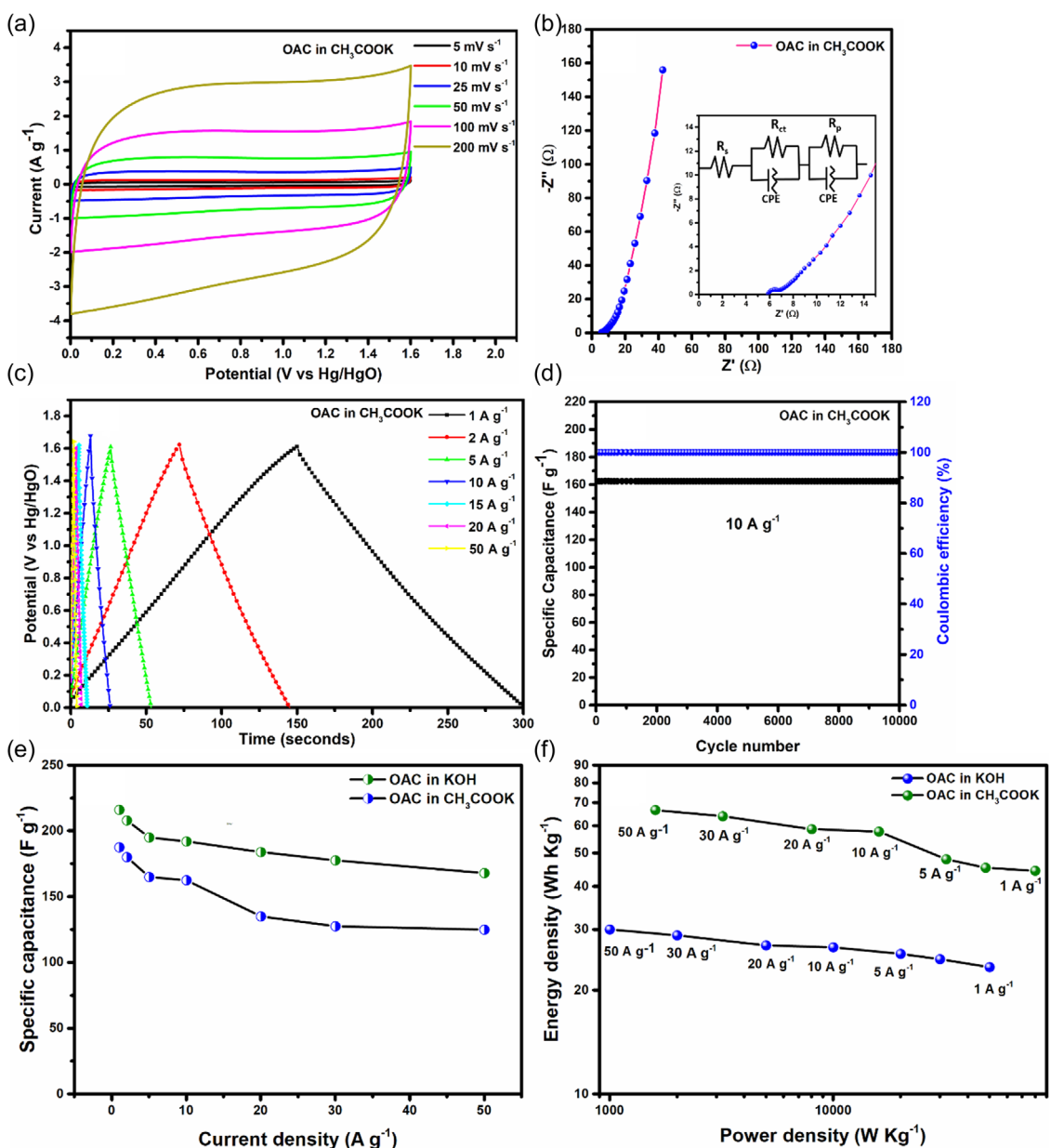


**Figure 8.** Electrochemical characterization of OAC electrode performed in 27 molal  $\text{CH}_3\text{COOK}$  aqueous electrolyte. a) CV curves at scan rates from  $5 \text{ mV s}^{-1}$  to  $200 \text{ mV s}^{-1}$ , b) Nyquist plot and (inset plot highlighting high-frequency region and electrochemical equivalent circuit model for EIS spectra), c) GCD curves from  $1 \text{ A g}^{-1}$  to  $50 \text{ A g}^{-1}$  current density, d) cyclic stability at a current density of  $10 \text{ A g}^{-1}$ , e) specific capacitance for varying current densities showing rate capability and, and f) Ragone plot showing the variation in electrochemical performance in terms of energy and power densities from  $1 \text{ A g}^{-1}$  to  $50 \text{ A g}^{-1}$  in two-electrode setup.

greater ionic size and high concentration, which result in ion–ion interactions hindering the movement of ions, consequently increasing resistance to current flow. In comparison, the charge transfer resistance ( $R_{ct} = 1 \Omega$ ) was very low. Notably, the quarter circle observed instead of a semicircle suggests limited ion diffusion. Compared to EIS spectrum of OAC in KOH electrolyte, the Warburg region observed here is slightly longer due to poor ionic mobility within the electrolyte.<sup>[64]</sup> In low-frequency region, a near- $90^\circ$  slope of EIS curve indicates ideal capacitive behavior.<sup>[61]</sup>

In Figure 8c, the perfect triangular shapes of GCD plots demonstrates symmetric and high reversibility of charge–discharge cycles. Even under increased current density, linear charging

and discharging behavior is maintained. A specific capacitance of  $185 \text{ F g}^{-1}$  is achieved at a current density of  $1 \text{ A g}^{-1}$  with enhanced energy density of  $65.77 \text{ Wh Kg}^{-1}$  at a power density of  $1600 \text{ W Kg}^{-1}$ . Table S3, Supporting Information shows the comparison of specific capacitance, energy density, and power density of OAC 2 electrode device using KOH and  $\text{CH}_3\text{COOK}$  as electrolytes. It is evident from Table S3, Supporting Information that the capacitance remains high even at elevated current densities, reaching  $125 \text{ F g}^{-1}$  at  $50 \text{ A g}^{-1}$ , with an appreciable energy density and extremely high power density ( $44.44 \text{ Wh Kg}^{-1}$  at  $80 \text{ KW Kg}^{-1}$ ). Figure 8d depicts that OAC exhibits excellent cyclic stability with 100% capacity retention at a steady capacitance of  $162.5 \text{ F g}^{-1}$  with

**Table 2.** Comparison of electrochemical performances at high current densities in the case of different types of electrode materials.

Sr no.	Carbon precursor	Surface area [ $\text{m}^2 \text{g}^{-1}$ ]	Aqueous electrolyte	Specific capacitance [ $\text{F g}^{-1}$ ] @ current density	Energy density [ $\text{Wh Kg}^{-1}$ ] @ current density	Power density [ $\text{W Kg}^{-1}$ ] @ current density	Ref.
1	Longan seeds	1732	Composite electrolyte	348 @ 0.5 $\text{A g}^{-1}$	10.2 @ 50 $\text{A g}^{-1}$	20,400 @ 50 $\text{A g}^{-1}$	[5]
2	Garlic skin	2818	6 M KOH	427 @ 0.5 $\text{A g}^{-1}$	11.18 <sup>a)</sup> @ 50 $\text{A g}^{-1}$	27,300 <sup>a)</sup> @ 50 $\text{A g}^{-1}$	[69]
3	Oily sludge	2561	6 M KOH	348 @ 0.5 $\text{A g}^{-1}$	7.22 @ 20 $\text{A g}^{-1}$	100,000 @ 20 $\text{A g}^{-1}$	[66]
4	Plant tissue (OPC)	2342	6 M KOH	365 @ 1 $\text{A g}^{-1}$	33 <sup>a)</sup> @ 50 $\text{A g}^{-1}$	210,000 <sup>a)</sup> @ 50 $\text{A g}^{-1}$	[25]
5	Graphene hydrogels	778–951	5 M KOH	220 @ 1 $\text{A g}^{-1}$	5.7 @ 100 $\text{A g}^{-1}$	30,000 @ 100 $\text{A g}^{-1}$	[60]
6	Bamboo byproducts	1472	6 M KOH	301 @ 0.1 $\text{A g}^{-1}$	6.1 @ 100 $\text{A g}^{-1}$	26,000 @ 100 $\text{A g}^{-1}$	[30]
7	Corn derivatives	1804	6 M KOH	411 @ 1 $\text{A g}^{-1}$	20 @ 30 $\text{A g}^{-1}$	28,010 @ 30 $\text{A g}^{-1}$	[67]
8	Petroleum asphalt	1093	6 M KOH	302 @ 1 $\text{A g}^{-1}$	10.42 @ 50 $\text{A g}^{-1}$	12,500 @ 50 $\text{A g}^{-1}$	[68]
9	Graphene/Pt	229	1 M $\text{H}_2\text{SO}_4$	249 @ 0.1 $\text{A g}^{-1}$	16.9 <sup>a)</sup> @ 50 $\text{A g}^{-1}$	22,500 <sup>a)</sup> @ 50 $\text{A g}^{-1}$	[70]
10	American poplar tree fruits	942	6 M KOH	423 @ 1 $\text{A g}^{-1}$	44 @ 50 $\text{A g}^{-1}$	25,157 @ 50 $\text{A g}^{-1}$	[71]
11	Okra	2109	6 M KOH	318 @ 1 $\text{A g}^{-1}$	23.3 @ 50 $\text{A g}^{-1}$	50,000 @ 50 $\text{A g}^{-1}$	This work
			27 molal $\text{CH}_3\text{COOK}$	256.8 @ 1 $\text{A g}^{-1}$	44.44 @ 50 $\text{A g}^{-1}$	80,000 @ 50 $\text{A g}^{-1}$	

<sup>a)</sup>Energy density and power density values were reported for three-electrode system.

100% coulombic efficiency. Thus, we find that, similar to results obtained with KOH electrolyte, OAC shows good rate capability in  $\text{CH}_3\text{COOK}$  electrolyte solution as well. The high rate capability can be mainly attributed to the purely EDLC charge storage mechanism observed for OAC samples. The hierarchical porous structure of OAC with an optimum combination of micro-, meso-, and macropores also aids in capacity retention by allowing better flow kinetics.<sup>[59]</sup>

Figure S9a,b, Supporting Information depicts the graphical representation of the correlation between current density and specific capacitance, energy density, and power density for OAC in KOH and  $\text{CH}_3\text{COOK}$  solutions as electrolytes in a three-electrode setup. Similar relation is shown in Figure 8e,f for two-electrode setup. As discussed previously, the specific capacitance values obtained in  $\text{CH}_3\text{COOK}$  are lower than the ones obtained with KOH electrolyte due to the difference in ionic radii of the anions. However, the profiles of graphs for capacitance versus current density in both electrolytes are almost identical (Figure 8e), indicating similar rate capability in both electrolytes. Figure 8f shows that the curves for energy density versus power density in both electrolytes also showed a similar trend. The increase in the potential window resulting from the use of  $\text{CH}_3\text{COOK}$  as an electrolyte improved the energy density and power density, as evident from both three-electrode and two-electrode data. Overall, based on the comparison of various electrochemical studies carried out with KOH and  $\text{CH}_3\text{COOK}$  as electrolytes, we do not see a significant impact of change in the electrolyte on electrochemical kinetics and charge storage mechanism which can be credited to the hierarchical porosity. However, the use of  $\text{CH}_3\text{COOK}$  as an electrolyte helped in enhancing the energy density and power density.

Very few studies have explored electrochemical performance of electrode materials for EDLC-type supercapacitors at very high current densities. **Table 2** provides a selection of references for comparison with our work. It is evident from the data that OAC demonstrates superior electrochemical performance compared to a range of carbon-based materials reported for

supercapacitor applications. Based on the data presented in Table 2, we can see that high surface area is not the only attribute that dictates the electrochemical performance.<sup>[65]</sup> For example, carbon derived from garlic skin,<sup>[66]</sup> oily sludge,<sup>[67]</sup> and plant tissues<sup>[25]</sup> all have a higher surface area than OAC presented in this study. However, electrochemical performance is inferior in the case of carbon derived from garlic peel and oily sludge and comparable in plant tissue-derived carbon. Thus, apart from the surface area, pore size distribution, electronic conductivity, and the nature of electrolytes play a crucial role. A good example of the effect of change in the electrolytes is bamboo-derived carbon mentioned in the table.<sup>[68]</sup> In this case, the authors switched from an aqueous electrolyte to an ionic liquid, which increased the potential window from 1 V to 3.5 V. Consequently, the energy density increased (6.1–43.3  $\text{Wh Kg}^{-1}$ ). Based on the comparison with the literature reports, we believe that the multifaceted approach used by us involving attention to precursor selection, surface area enhancement, pore engineering, and electrolyte selection leads to excellent electrochemical performance of OAC.

### 3. Conclusion

In this study, we have successfully demonstrated a strategic, multipronged approach for the development of high-performance supercapacitor materials using OAC. The intrinsic properties of okra, notably its high water and mineral content, played a pivotal role in enabling unique pore engineering strategies involving sequential processing steps. For example, the natural hierarchical structure was preserved through freeze-drying. Ash removal and microporosity enhancement of pre-carbonized okra were achieved through acid treatment. Further, enhanced activation of OAT was achieved through impregnation and aging of OAT with KOH solution. As a result, the obtained activated carbon exhibited an ultrahigh specific surface area of  $2109 \text{ m}^2 \text{ g}^{-1}$  and a significant pore volume of  $1.091 \text{ cc g}^{-1}$ , with a well-balanced

micropore/mesopore/macropore distribution, where 60/40 micropore/mesopore volume ratio and macropores provide a large number of accessible electroactive sites. Furthermore, nitrogen and oxygen codoping effectively introduced surface defects, thereby increasing the density of electroactive sites. Electrochemical investigations confirmed the dominant EDLC behavior of the OAC, delivering a high specific capacitance of  $318 \text{ F g}^{-1}$  at  $1 \text{ A g}^{-1}$  in 6 M KOH electrolyte. An innovative aspect of this work was the use of a WiSE (27 M  $\text{CH}_3\text{COOK}$ ), which extended the operational voltage window to 1.6 V in aqueous systems achieving a high energy density of  $44.44 \text{ Wh kg}^{-1}$  and a remarkable power density of  $80,000 \text{ W kg}^{-1}$  at  $50 \text{ A g}^{-1}$  while maintaining excellent cyclic stability with 100% capacitance retention over 10 000 cycles. This research work focusses on the importance of combining prudent precursor selection, structural preservation, tailored processing steps, and strategic electrolyte optimization to simultaneously achieve superior energy and power densities in aqueous supercapacitors. The methodologies and insights presented here offer a scalable and effective framework for developing next-generation, biomass-derived energy storage materials with enhanced electrochemical performance of supercapacitors.

## 4. Experimental Section

### Materials and Reagents

Raw okra procured from local farms around Hyderabad, India was used as a carbon precursor. For activation and further treatment of carbonized okra, potassium hydroxide pellets (KOH; SRL; 85% assay) and nitric acid ( $\text{HNO}_3$ ; Qualigens (ThermoFisher scientific); 70% assay) were used. For the preparation of the electrode: polyvinylidene difluoride (PVDF, Sigma-Aldrich), carbon black (super P-65), dimethylformamide (DMF), and graphite sheet; KOH and  $\text{CH}_3\text{COOK}$  (SRL; 99% assay) as a solute and Millipore water (DI) water having a resistance of  $18.2 \text{ M}\Omega\text{cm}$  at room temperature (i.e.  $25^\circ\text{C}$ ) as a solvent used for the preparation of electrolyte solution.

### Fabrication Procedure of OAC

The synthesis process is depicted schematically in Figure 1. Okra pods were initially cleansed with ethanol and DI water multiple times to eliminate any surface impurities. Then, the pods were diced into small fragments. For freeze-drying, the okra fragments were flash-frozen in liquid nitrogen until solid, followed by a 52 h freeze-drying process using a Telstar Freeze Dryer Model: Telstar Lyoquest-85 (Sl. no. 3850). The resultant freeze-dried material was precarbonized in a tubular furnace at  $500^\circ\text{C}$  for 1 h under an argon atmosphere, with a heating rate of  $5^\circ\text{C}$  per minute, yielding precarbonized okra (OC) in the form of biochar. To remove inorganic mineral ash residues formed during carbonization, the ground OC underwent acid treatment using 3 M  $\text{HNO}_3$  (200 mg carbon in 30 mL of  $\text{HNO}_3$  solution) and was stirred for 12 h. Subsequently, the acid-treated precarbonized okra (OAT) was rinsed multiple times with DI water until reaching a pH of 7. The resulting sample was then dried in a hot-air oven for 15 h at  $100^\circ\text{C}$ . The biochar produced is highly amorphous with disordered carbon, facilitating easy accessibility and penetration of activating agents into all sites. The activation of OAT was carried out by making a concentrated solution by immersing a mixture of KOH and OAT in a weight ratio (1:1) in DI water (200 mg OAT in 10 mL DI water). The resulting slurry was stirred for 12 h and left undisturbed for

4 days to allow complete wetting of the char, enabling sufficient time for KOH infusion into the carbon matrix. Subsequently, the mixture was air-dried using a hot-air oven at  $100^\circ\text{C}$  for 15 h, ground thoroughly, and further heat-treated in the tubular furnace at  $1000^\circ\text{C}$  for 1 h under an argon atmosphere at a heating rate of  $5^\circ\text{C}$  per minute. The resulting activated carbon, termed OAC, was then washed multiple times with 3M  $\text{HNO}_3$ , followed by DI water to eliminate any remaining KOH decomposition products and neutralize basicity.

### Sample Characterization

The morphology and microstructure of the material were characterized by field emission SEM (FE-SEM) (Carle Zeiss SUPRA 40 and Thermo Scientific Axis ChemiSEM; operated at 20 kV) and high-resolution TEM (HR-TEM) (JEOL JEM 2100; operated at 200 kV) for high-resolution images. For TEM analysis, the sample was ground to a fine powder and dispersed in ethanol, followed by ultrasonication, and then drop cast over the carbon-coated copper grid. Powder XRD was performed on D8 Advance BRUKER, installed with incident radiation Cu K $\alpha$  having wavelength ( $\lambda$ ) of  $1.54 \text{ \AA}$ , at a scan rate of  $1^\circ$  per minute. Specific surface area and pore volume distribution were analyzed through a nitrogen sorption study using BET analysis (Autosorb iQ, Quantachrome). Prior to analysis, the samples were degassed at  $100^\circ\text{C}$  for 12 h. Elemental and compositional investigation of OAC is done by EDS. To check thermal stability and carbon yield, thermogravimetric analysis was conducted using the SDT Q600 V20.9 Build 20 instrument, exposing the sample up to  $900^\circ\text{C}$  temperature in an air atmosphere.

The nature of bonding and identification of functional groups was done by XPS analysis (X-Ray photoelectron spectrometer equipment; Shimazu group company, AXIS supra, C322905/01, aluminum source); Raman spectra with a laser source of  $532 \text{ nm}$  wavelength were recorded using Bruker SENTERRA micro-Raman spectrometer.

### Electrochemical Study

Electrochemical behavior was studied with the help of a three-electrode setup in a bath cell using platinum as a counter electrode and saturated calomel electrode as a reference electrode. Device-level testing was conducted using a two-electrode configuration in a Swagelok cell setup, incorporating a glass fiber separator (Whatman Glass Microfibre filters, Cat. no. 1823-150, 150 mm diameter,  $650 \mu\text{m}$  thickness). For the preparation of the working electrode, activated carbon (OAC), PVDF as a binder, and carbon black as a conductive material were mixed in the weight ratio of 8:1:1. To this mixture, DMF was added as a solvent, and the resultant suspension was ball milled for 3 h at 150 rpm to obtain a homogeneous and viscous slurry. A thin layer of OAC slurry was coated over the graphite sheet and further dried in a hot-air oven for 15 h. Electrochemical studies (CV, GCD, EIS) were carried out using AUTOLAB (PGSTAT302N: -AUT87846) with the help of NOVA 2.1 software. From the galvanostatic charge-discharge plot, the specific capacitance in  $\text{F g}^{-1}$  was calculated using the equation (6) and (7).

$$C_s = \frac{I_m x \Delta t}{\Delta V} \quad (\text{for three - electrode system}) \quad (6)$$

$$C_s = 2x \frac{I_m x \Delta t}{\Delta V} \quad (\text{for two - electrode system}) \quad (7)$$

where  $C_s$  is the specific capacitance,  $\Delta t$  (second) is the discharge time,  $m$  (gram) is the active mass coated on the working electrode,  $\Delta V$  (V) is a potential window, and  $I_m$  ( $\text{A g}^{-1}$ ) is the current density. The energy density and power density of the material were estimated by using Equation (8) and (9), respectively, as mentioned below.

$$E (\text{Wh kg}^{-1}) = \frac{1}{2} C_s (\Delta V)^2 \times \frac{1000}{3600} = \frac{C_s x (\Delta V)^2}{7.2} \quad (8)$$

$$P (\text{W kg}^{-1}) = \frac{E}{\Delta t} * 3600 \quad (9)$$

Here,  $E$  ( $\text{Wh kg}^{-1}$ ) represents the specific energy density and  $P$  ( $\text{W kg}^{-1}$ ) denotes the specific power density.  $\Delta V$  signifies the cell voltage range during both the charging and discharging processes, while  $\Delta t$  denotes the discharge time measured in seconds.<sup>[17]</sup>

## Acknowledgements

The authors are grateful to Dr. Narendra Kurra and Dr. Sai Rama Krishna Malladi for their help and guidance with electrochemical characterization. The authors also thank the Ministry of Education (MoE) India and Indian Institute of Technology Hyderabad, India (IITH) for financial support.

## Conflict of Interest

The authors declare no conflict of interest.

## Author Contributions

**Ekta Majhi:** conceptualization (equal); data curation (lead); formal analysis (lead); investigation (lead); methodology (equal); software (lead); validation (equal); visualization (lead); writing—original draft (lead); writing—review & editing (equal). **Atul S. Deshpande:** conceptualization (equal); Funding acquisition (lead); methodology (lead); Project administration (lead); Resources (lead); Supervision (lead); validation (lead); writing—review & editing (lead).

## Data Availability Statement

The data that support the findings of this study are available from the corresponding author upon reasonable request.

**Keywords:** energy density • hierarchically porous • okra-derived activated carbon • power density • water-in-salt electrolytes

- [1] V. Aravindan, J. Gnanaraj, Y. S. Lee, S. Madhavi, *Chem. Rev.* **2014**, *114*, 11619.
- [2] S. Sundriyal, V. Shrivastav, H. D. Pham, S. Mishra, A. Deep, D. P. Dubal, *Resour. Conserv. Recycl.* **2021**, *169*, 105548.
- [3] K. K. Patel, T. Singh, V. Pandey, T. P. Sumangala, M. S. Sreekanth, *J. Energy Storage* **2021**, *44*, 2352.
- [4] J. Shi, B. Jiang, Z. Liu, C. Li, F. Yan, X. Liu, H. Li, *Ceram. Int.* **2021**, *47*, 18540.
- [5] D. Zhang, B. Yang, W. She, S. Gao, J. Wang, Y. Wang, K. Wang, H. Li, L. Han, *J. Power Sources* **2021**, *506*, 230103.
- [6] N. K. Rotte, V. Naresh, S. Muduli, V. Reddy, V. V. S. Srikanth, S. K. Martha, *Electrochim. Acta* **2020**, *363*, 137209.
- [7] Y. Gao, Q. Wang, G. Ji, A. Li, J. Niu, *RSC Adv.* **2021**, *11*, 5361.
- [8] G. Lin, R. Ma, Y. Zhou, Q. Liu, X. Dong, J. Wang, *Electrochim. Acta* **2018**, *261*, 49.
- [9] Q. Dou, H. S. Park, *Energy Environ. Mater.* **2020**, *3*, 286.
- [10] V. S. Bhat, S. S. T. J. Jayeoye, T. Rujiralai, U. Sirimahachai, K. F. Chong, G. Hegde, *Nano. Select.* **2020**, *1*, 226.
- [11] B. Yan, J. Zheng, L. Feng, Q. Zhang, C. Zhang, Y. Ding, J. Han, S. Jiang, S. He, *Mater. Des.* **2023**, *229*, 111904.
- [12] Q. L. Chen, K. H. Xue, W. Shen, F. F. Tao, S. Y. Yin, W. Xu, *Electrochim. Acta* **2004**, *49*, 4157.
- [13] J. S. Chae, W. S. Kang, K. C. Roh, *Energies Basel* **2021**, *14*, 5990.
- [14] Y. H. Chiu, L. Y. Lin, *J. Taiwan Inst. Chem. Eng.* **2019**, *101*, 177.
- [15] Y. Zhang, Y. P. Zhao, L. L. Qiu, J. Xiao, F. P. Wu, J. P. Cao, Y. H. Bai, F. J. Liu, *Diamond Relat. Mater.* **2022**, *129*, 109331.
- [16] J. Cheng, S. C. Hu, G. T. Sun, K. Kang, M. Q. Zhu, Z. C. Geng, *Energy* **2021**, *215*, 119144.
- [17] M. Usha Rani, K. Nanaji, T. N. Rao, A. S. Deshpande, *J. Power. Sources* **2020**, *471*, 228387.
- [18] N. Guo, M. Li, Y. Wang, X. Sun, F. Wang, R. Yang, *ACS Appl. Mater. Interfaces* **2016**, *8*, 33626.
- [19] L. Feng, H. Liu, W. Zan, S. Li, Y. Chang, Y. Zhang, W. Hou, Y. Zhao, S. Zhu, G. Han, *Chem. Eng. J.* **2024**, *486*, 1385.
- [20] X. Tian, Q. Zhu, B. Xu, *ChemSusChem* **2021**, *14*, 2501.
- [21] R. J. Mo, Y. Zhao, M. Wu, H. M. Xiao, S. Kuga, Y. Huang, J. P. Li, S. Y. Fu, *RSC Adv.* **2016**, *6*, 59333.
- [22] F. Fei, H. Zhou, C. Gu, M. Kang, *Colloids Surf. A Physicochem. Eng. Asp.* **2022**, *654*, 130061.
- [23] M. R. Pallavolu, K. G. Krishna, G. Nagaraju, P. S. S. Babu, S. Sambasivam, A. Sreedhar, *J. Ind. Eng. Chem.* **2022**, *160*, 428.
- [24] F. Wang, X. Liu, G. Duan, H. Yang, J. Y. Cheong, J. Lee, J. Ahn, Q. Zhang, S. He, J. Han, Y. Zhao, I. D. Kim, S. Jiang, *Small* **2021**, *17*, 2102532.
- [25] J. Li, Y. Gao, K. Han, J. Qi, M. Li, Z. Teng, *Sci. Rep.* **2019**, *9*, 17270.
- [26] A. Adan-Mas, L. Alcaraz, P. Arévalo-Cid, F. A. López-Gómez, F. Montemor, *Waste Manag.* **2021**, *120*, 280.
- [27] B. Wang, Y. Wang, Y. Peng, X. Wang, J. Wang, J. Zhao, *J. Power Sources* **2018**, *390*, 186.
- [28] K. Subramani, N. Sudhan, M. Karnan, M. Sathish, *ChemistrySelect* **2017**, *2*, 11384.
- [29] X. Kong, Y. Zhang, P. Zhang, X. Song, H. Xu, *Appl. Surf. Sci.* **2020**, *516*, 146162.
- [30] W. Tian, Q. Gao, Y. Tan, K. Yang, L. Zhu, C. Yang, H. Zhang, *J. Mater. Chem. A* **2015**, *3*, 5656.
- [31] W. Sun, S. M. Lipka, C. Swartz, D. Williams, F. Yang, *Carbon* **2016**, *103*, 181.
- [32] P. Dhanasekaran, D. R. Kumar, J. J. Shim, D. Kalpana, *New J. Chem.* **2022**, *46*, 7433.
- [33] C. Peng, X. B. Yan, R. T. Wang, J. W. Lang, Y. J. Ou, Q. J. Xue, *Electrochim. Acta* **2013**, *87*, 401.
- [34] M. Sevilla, W. Gu, C. Falco, M. M. Titirici, A. B. Fuertes, G. Yushin, *J. Power Sources* **2014**, *267*, 26.
- [35] B. Wang, X. Wu, Y. Yu, N. Wang, Z. Zhou, *Electrochim. Acta* **2022**, *432*, 141219.
- [36] Q. Kang, L. Appels, T. Tan, R. Dewil, *Sci. World J.* **2014**, *2014*, 298153.
- [37] H. F. Gemedo, G. D. Hak, F. Beyene, A. Z. Woldegiorgis, S. K. Rakshit, *Food Sci. Nutr.* **2016**, *4*, 223.
- [38] D. Damodar, S. Ghosh, U. Rani, S. Kumar Martha, A. S. Deshpande, *J. Power Sources* **2019**, *438*, 227008.
- [39] P. Kale, *Int. J. Sci. Dev. Res.* **2013**, *6*, 168.
- [40] Y. Liu, Z. Shi, Y. Gao, W. An, Z. Cao, J. Liu, *ACS Appl. Mater. Interfaces* **2016**, *8*, 28283.
- [41] U. Farooq, R. Malviya, P. Kumar Sharma, *Acad. J. Plant Sci.* **2013**, *6*, 168.
- [42] H. HosseiniZadeh, M. Sadeghzadeh, M. Babazadeh, *J. Biomater. Nanobiotechnol.* **2011**, *2*, 311.
- [43] P. R. Chauhan, G. Raveesh, K. Pal, R. Goyal, S. K. Tyagi, *Biore sour. Technol. Rep.* **2023**, *22*, 101425.
- [44] M. Thommes, K. Kaneko, A. V. Neimark, J. P. Olivier, F. Rodriguez-Reinoso, J. Rouquerol, K. S. W. Sing, *Pure. Appl. Chem.* **2015**, *87*, 1051.
- [45] V. Uskoković, *Carbon Trends* **2021**, *5*, 100116.
- [46] A. C. Ferrari, J. Robertson, *Phys. Rev. B* **2000**, *61*, 14095.
- [47] K. Zafer, S. Zainab, M. Masood, M. Sohail, S. S. A. Shah, M. R. Karim, A. O'Mullane, K. Ostrikov, G. Will, M. A. Wahab, *Chem. Rec.* **2024**, *24*, 1144.
- [48] J. B. Wu, M. L. Lin, X. Cong, H. N. Liu, P. H. Tan, *Chem. Soc. Rev.* **2018**, *47*, 1822.
- [49] Z. Xu, X. Zhuang, C. Yang, J. Cao, Z. Yao, Y. Tang, J. Jiang, D. Wu, X. Feng, *Adv. Mater.* **2016**, *28*, 1981.
- [50] D. Damodar, S. Kumar, S. K. Martha, A. S. Deshpande, *Dalton Trans.* **2018**, *47*, 12218.
- [51] M. U. Rani, V. Naresh, D. Damodar, S. Muduli, S. K. Martha, A. S. Deshpande, *Electrochim. Acta* **2021**, *365*, 137284.

- [52] R. Zhao, X. Yang, Z. She, Q. Wu, K. Shi, Q. Xie, Y. Ruan, *Energy Fuels.* **2023**, *37*, 3110.
- [53] A. Ilnicka, M. Skorupska, M. Szkoda, A. M. Kolanowska, M. Trykowski, A. Wróblewska, M. Ziolek, *Sci. Rep.* **2021**, *11*, 18387.
- [54] M. R. Lukatskaya, J. I. Feldblum, D. G. Mackanic, F. Lissel, D. L. Michels, Y. Cui, Z. Bao, *Energy Environ. Sci.* **2018**, *11*, 2876.
- [55] T. S. Mathis, N. Kurra, X. Wang, D. Pinto, P. Simon, Y. Gogotsi, *Adv. Energy Mater.* **2019**, *9*, 1902007.
- [56] K. Sharma, P. Kadyan, R. K. Sharma, S. Grover, *J. Energy Storage* **2024**, *100*, 113679.
- [57] D. Zhu, J. Jiang, D. Sun, X. Qian, Y. Wang, L. Li, Z. Wang, X. Chai, L. Gan, M. Liu, *J. Mater. Chem. A* **2018**, *6*, 12334.
- [58] Y. Ma, D. Chen, Z. Fang, Y. Zheng, W. Li, S. Xu, X. Lu, G. Shao, Q. Liu, W. Yang, *PNAS* **2021**, *118*, 2106510118.
- [59] L. Zhang, G. Shi, *J. Phys. Chem. C* **2011**, *115*, 17206.
- [60] P. Suktha, P. Chiochan, P. Lampraserkun, J. Wuttiprom, N. Phattharasupakun, M. Suksomboon, T. Kaewsongpol, P. Sirisinudomkit, T. Pettong, M. Sawangphruk, *Electrochim. Acta.* **2015**, *176*, 504.
- [61] J. Zhu, M. Yanilmaz, K. Fu, C. Chen, Y. Lu, Y. Ge, D. Kim, X. Zhang, *J. Memb. Sci.* **2016**, *504*, 89.
- [62] J. Li, H. Jia, S. Ma, L. Xie, X. X. Wei, L. Dai, H. Wang, F. Su, C. M. Chen, *ACS Energy Lett.* **2023**, *8*, 56.
- [63] S. H. Ma, Q. Yin, J. P. Zhao, *J. Electrochem.* **2024**, *30*, 2408051.
- [64] T. Hori, C. Mabuchi, T. Kinoshita, M. Nakauchi, Y. Yoshimoto, *J. Electrochem. Soc.* **2018**, *165*, 826.
- [65] S. Kumar, E. Majhi, A. S. Deshpande, M. Khandelwal, *Carbon Trends* **2024**, *16*, 100385.
- [66] X. Li, K. Liu, Z. Liu, Z. Wang, B. Li, D. Zhang, *Electrochim. Acta* **2017**, *240*, 43.
- [67] K. Kumar Reddy Reddyguntla, R. Beresford, L. Berlouis, A. Ivaturi, *Energy Fuels.* **2023**, *37*, 19248.
- [68] W. Yang, B. Deng, L. Hou, J. Tian, Y. Tang, S. Wang, F. Yang, Y. Li, *Ind. Eng. Chem. Res.* **2019**, *58*, 4487.
- [69] Q. Zhang, K. Han, S. Li, M. Li, J. Li, K. Ren, *Nanoscale* **2018**, *10*, 2427.
- [70] D. Zhang, X. Zhang, Y. Chen, C. Wang, Y. Ma, H. Dong, L. Jiang, Q. Meng, W. Hu, *Phys. Chem. Chem. Phys.* **2012**, *14*, 45.
- [71] T. R. Kumar, R. A. Senthil, Z. Pan, J. Pan, Y. Sun, *J. Energy Storage* **2020**, *32*, 101903.

Manuscript received: March 6, 2025

Revised manuscript received: May 2, 2025

Version of record online: